CALICE Analysis Note CAN-034
June 4, 2011

Analysis of low-energetic electron and pion data collected with the AHCAL prototype at Fermilab

The CALICE Collaboration [1]

Abstract

This note presents the current status of the analysis of electron and pion data collected with the CALICE AHCAL (Analog Hadron Calorimeter) physics prototype at the Fermilab Test Beam Facility in 2008 and 2009. The experimental setup, the operation of the Čerenkov detector, the calibration of the AHCAL data, and the identification of bad cells are explained. The event selection criteria for electron and pion data and the purities of these samples are presented. Linearity and resolution of the electromagnetic response are investigated. The results are compared to the results obtained for the CERN data. Finally, the AHCAL response to negative pions and the ratio between this response and the electromagnetic response ($\frac{\pi}{e}$ ratio) are shown.

[1] Author: Nils Feege; nils.feege@desy.de

Contents

1 Introduction

This note presents the current status of the analysis of electron and pion data collected with the AHCAL (Analog Hadron Calorimeter, [1]) physics prototype at the Fermilab Test Beam Facility in 2008 and 2009. The first sections give a brief overview over the experimental setup and describe the operation of the Čerenkov detector, the AHCAL calibration, and the identification method for bad cells. The next sections cover the event selection criteria for electron and pion data and the purities of these samples. The last sections present the analysis results for electron and pion data. The electron data allow for extending the range of linearity and resolution studies down to 1 GeV (beam energy and momentum are used interchangeably throughout this text). Previous positron analyses presented in [2] use data from CERN 2007 and cover the range from 10 GeV to 50 GeV. The negative pion data used in this note range from 1 GeV to 30 GeV and will provide a good basis for future comparisons between data and Monte Carlo simulations. Finally, the $\frac{\pi}{e}$ ratio for the AHCAL between 1 GeV and 20 GeV is shown.

2 Experimental setup at the Fermilab Test Beam Facility

The CALICE detector prototypes and auxiliary beam line instrumentation were installed in the MT6-2 area of the MTest beam line at the Fermilab Test Beam Facility [3]. Figure 1 shows the arrangement of the single components. All devices were centered on the nominal beam axis.

The AHCAL prototype resided on a movable stage. This stage allowed for moving the detector in x- and y-direction (i.e. orthogonal to the beam axis) and to rotate and stagger it by up to 30 degrees in the x-z-plane. The TCMT (Tail Catcher and Muon Tracker) was located behind the AHCAL.

A set of scintillators with photomultiplier tube (PMT) readout provided information for triggering the data acquisition and about the beam quality. The main trigger for charged particles was the coincidence between the signals from two $10 \times 10\,\mathrm{cm}^2$ scintillators. For collecting muon data, the coincidence between the signals from two $1 \times 1\,\mathrm{m}^2$ scintillators was used instead. The upstream $1 \times 1\,\mathrm{m}^2$ scintillator was only installed during muon measurements, while the downstream scintillator was kept as a veto for muon events. The analog signal from a $20 \times 20\,\mathrm{cm}^2$ scintillator (called multiplicity counter) was used to identify events with two or more particles passing through the scintillator simultaneously. In addition, this scintillator was an alternate trigger for charged particles. A veto trigger allowed for identifying events with additional particles in the beam halo or particles that initiated a shower before reaching the AHCAL. The veto trigger was a $1 \times 1\,\mathrm{m}^2$ scintillator plane with a $20 \times 20\,\mathrm{cm}^2$ hole in its center. The plane was pieced together from four scintillator planes measuring $60 \times 40\,\mathrm{cm}^2$ each.

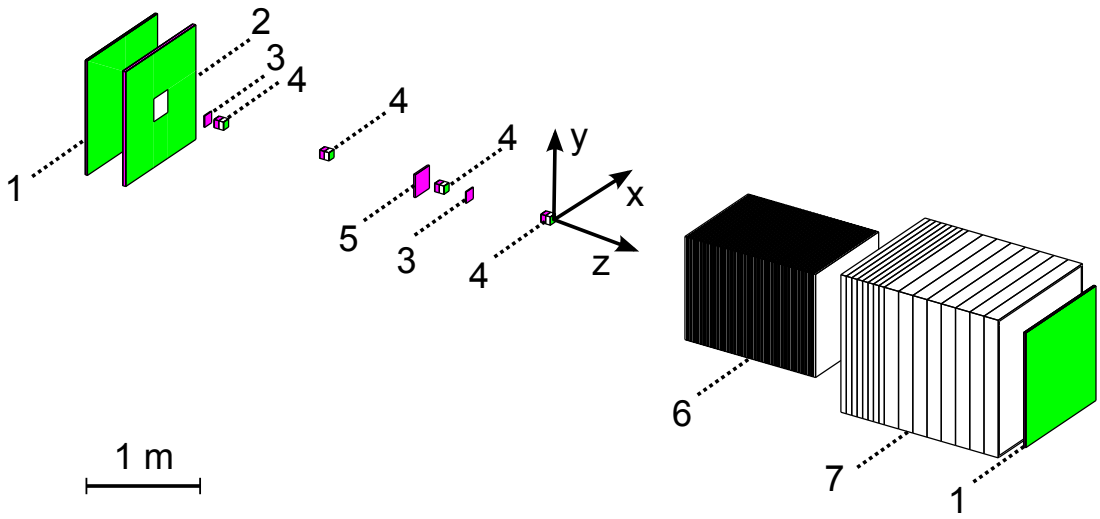

Figure 1: The experimental setup at MTest: (1) $1 \times 1\,\mathrm{m}^2$ scintillators, (2) $1 \times 1\,\mathrm{m}^2$ veto wall, (3) $10 \times 10\,\mathrm{cm}^2$ scintillators, (4) drift chambers, (5) $20 \times 20\,\mathrm{cm}^2$ multiplicity counter, (6) AHCAL, (7) TCMT.

Four drift chambers measured the position of the charged beam particles. The center of the backplane of the most downstream drift chamber defines the origin of the global CALICE coordinate system.

The secondary beams provided at the Fermilab Test Beam Facility comprised charged particles of various types. Most particles were electrons, pions, or muons for positive beams and positrons, pions, muons, or protons for positive beams [3]. The MTest beam line instrumentation provided a differential Čerenkov detector, which allowed the identification of these particles based on the differences of their masses. Section 3 covers this device and its operation. The information from the Čerenkov detector was included in the on-line trigger decision to enhance the electron, pion or proton content in the recorded data. The distance between the downstream end of the Čerenkov detector and the most downstream CALICE drift chamber was 29 m.

3 The differential Čerenkov detector at MTest

Charged particles with momentum p emit Čerenkov light when passing through a medium of refractive index n if their mass m lies below the threshold mass m_{thr}. This threshold is given by

$$m_{\mathrm{thr}} = \frac{p}{c} \cdot \sqrt{n^2 - 1}\,, \tag{1}$$

where c is the speed of light in vacuum. The opening angle θ_{cone} of the Čerenkov light cone is proportional to $\Delta m = (m_{\mathrm{thr}} - m)$. Figure 2 sketches the layout of the differential Čerenkov counter used at MTest. The Čerenkov light was generated in an 18.5 m long pressure tank. The tank could be filled with Nitrogen or Helium with pressures up to

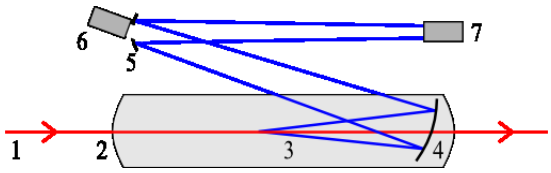

(a)

Figure 2: The differential Čerenkov counter at MTest: (1) incoming particle, (2) pressure tank with gas, (3) Čerenkov light, (4) mirror, (5) mirror with hole, (6) inner PMT, (7) outer PMT.

1.36 atm (20 psia). We used only Nitrogen. A glass mirror inside the tank reflected the Čerenkov light to a second mirror, which had a hole in its center. For narrow Čerenkov light cones, the light shone through the hole on the inner photomultiplier tube. When the light cone was wider than the hole, the light was reflected further to the outer photomultiplier tube. The refractive index of gas is proportional to the gas pressure. Therefore, adjusting the gas pressure changes both $m_{\rm thr}$ and $\theta_{\rm cone}$. In addition, the Čerenkov light intensity (and thus the detection efficiency with the PMTs) increases with the gas pressure.

Figure 3 shows the fraction of negatively charged particles that traversed the Čerenkov volume and generated a signal in the inner or the outer PMT at different gas pressures. The gas tank was filled with Nitrogen and the beam momentum was 10 GeV. The total number of passing particles was determined by a scintillator placed right downstream of the pressure tank. At pressures below 5 psia (1 atm = 14.7 psia), the outer PMT only saw light from electrons (45% of the beam particles at this energy) while no signal was detected in the inner PMT. Between $5-6$ psia, the threshold mass rose above the pion and muon masses and the inner PMT started to see light as well. Due to their low mass differences, 10 GeV muons and pions could not be separated by this Čerenkov detector. At higher pressures, the difference between the masses of pions and muons and the mass threshold increased. The Čerenkov cones of these particles became wider and the light moved from the inner to the outer PMT. Within the pressure limit of the gas tank, 10 GeV kaons could not generate Čerenkov light.

Pressure scans were recorded for different beam momenta to extract the threshold pressure $P_{\rm T}^{\pi}$ where the inner PMT started to see light from pions (and muons). Figure 4(a) summarizes the results for beam momenta between 6 GeV and 30 GeV (the measurement errors smaller than the marker sizes). The theoretical prediction for the threshold pressure $P_{\rm T}$ of a particle with mass m is given by

$$P_{\rm T} = \frac{\frac{1}{\sqrt{1-\frac{m^2}{E^2}}} - 1}{\delta} + O \,, \qquad (2)$$

where $\delta = n_{\rm 1atm} - 1 = 0.000297$ (nitrogen) and $P_{\rm T}$ is in unit atm [3]. The offset O takes into account a systematic gauge uncertainty of the pressure sensor. The solid line in Fig. 4(a) shows the prediction of Eq. (2) after fitting the function to the pion measurements to determine the offset O of 0.8 psia (0.05 atm).

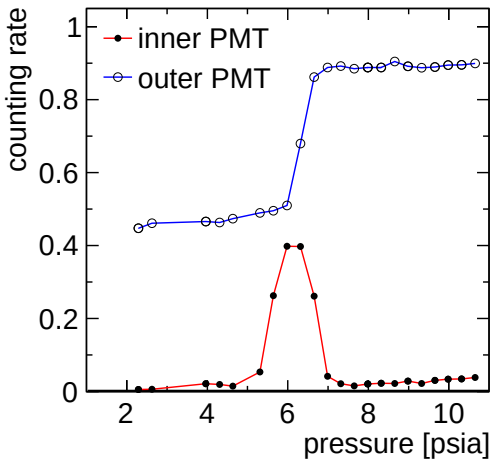

Figure 3: Čerenkov pressure scan using Nitrogen and negatively charged particles at 10 GeV beam momentum.

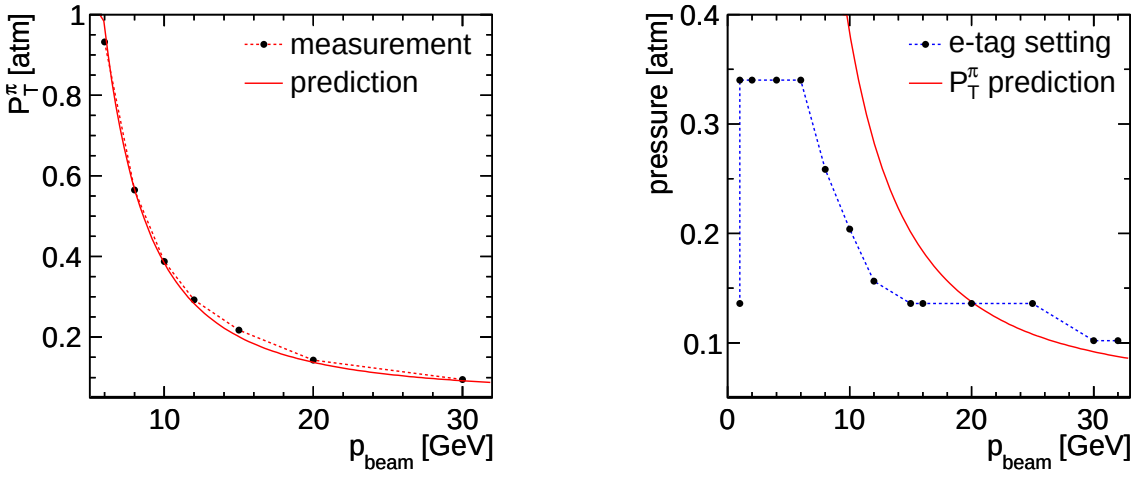

(a) (b)

Figure 4: (a) The measured threshold pressures for pions at different beam momenta. (b) Čerenkov detector operation pressure for enhancing the electron content in the recorded data at different beam momenta.

CALICE used the information from the Čerenkov detector in the on-line trigger decision to enhance the pion, electron or proton content in the recorded data. Pions were measured both with negative and positive beams, electrons with negative beams, and protons with positive beams. From 8 GeV to 30 GeV, pions were identified by setting the Čerenkov pressure to the pion threshold P_{T}^{π} and requiring a signal in the inner PMT. For pion momenta below 6 GeV, the threshold pressure exceeded the 1.36 atm pressure limit of the Čerenkov gas tank (Eq. (2) yields $P_{\mathrm{T}}^{\pi} = 1.37$ atm for 5 GeV pions, $P_{\mathrm{T}}^{\pi} = 2.12$ atm for 4 GeV pions, and $P_{\mathrm{T}}^{\pi} = 33.6$ atm for 1 GeV pions). Thus, the strategy for enhancing the pion content of the recorded data between 1 GeV and 4 GeV was to set the Čerenkov pressure to 1.36 atm and reject all events with a signal in the Čerenkov detector, i.e. all electrons (or positrons). This approach did not suppress kaon or (anti-)proton events, but the contribution from these particles to the beam at low momenta was small and could not be observed. At 6 GeV, both selection strategies were tested: First, the Čerenkov pressure was set to the threshold for 6 GeV pions and only events with a signal in the inner PMT were recorded. Afterwards, the Čerenkov pressure was set to 0.68 atm and events with a signal in any of the Čerenkov PMTs were rejected. The second approach yielded a 20% higher pion data acquisition rate than the first one at a comparable pion purity.

For enhancing the fraction of electron events in the collected data (negative beam), only events with a signal in the Čerenkov detector were recorded. Figure 4(b) presents the operation pressures applied for the electron selection from 1 GeV to 30 GeV. The red line is the theory prediction for the pion threshold from Eq. (2) (taking into account the measurement offset $O = 0.05$ atm). At 1 GeV, two pressure settings were used (0.34 atm and 0.14 atm). The lower setting reduced the material in the beam line while yielding a comparable data acquisition rate.

Protons were selected by setting the gas pressure to 1.36 atm and requiring no signal in the inner and the outer Čerenkov PMTs (positive beam). This selection suppressed positron, pion, and muon events for beam momenta down to 6 GeV. In addition, this approach rejected kaons above 18 GeV (Eq. (2) yields a threshold pressure for 18 GeV kaons of 1.31 atm).

4 Calibration and temperature correction

During the measurements at Fermilab in 2008 and 2009, the silicon photomultipliers (SIPMs) of the AHCAL prototype were operated at two different sets of bias voltages. The first set was used from May 2008 to the beginning of July 2008. In July, the bias voltages of all SIPMs were increased by 200 mV to compensate for a higher detector temperature. The adjusted voltage settings were applied in September 2008 and May 2009 as well. This note includes data from July 2008, September 2008, and May 2009. All these data were collected at the same operation voltages.

A full description of the AHCAL calibration procedure is given in [2]. The gains and inter-

calibration factors (i.e. the signal ratios between calibration mode and physics mode) for each cell were measured daily during the data collection periods. The measurements from July and September were averaged for calibrating the data. The mean temperature of the gain measurements was 26.5 °C. The mean gain of all SIPMs was 300 ADC counts per photon, the mean inter-calibration factor was 10 . These means were used for calibrating cells for which the corresponding measurements had failed.

The muon calibration factors were extracted from a set of muon measurements performed in September 2008 at an average detector temperature of 25.3 °C. The mean difference between the applied bias voltage and the breakdown voltage of all the SIPMs was 4 V. At these operation conditions, the mean light yield of all cells was 14.0 $\frac{\text{pixel}}{\text{MIP}}$. Only cells with a signal above a threshold of 0.5 MIP were used for analysis. These cells are called hits. With this threshold cut, the MIP detection efficiency of a single AHCAL cell was 93% [2].

The data used in this note were collected at an average detector temperature ranging from 24 °C to 28 °C. Thus, the gain and response variations of the SIPMs with temperature needed to be corrected for. An average temperature dependence of the gain of $-1.6\,\frac{\%}{\text{K}}$ and an average temperature dependence of the muon response of $-3.4\,\frac{\%}{\text{K}}$ was applied for correcting the calibration factors of all cells.

The gain-temperature dependence of $-1.6\,\frac{\%}{\text{K}}$ corresponds to the factor used for calibrating the CERN 2007 data ($-1.7\,\frac{\%}{\text{K}}$, [2]) after scaling this factor by the mean ratio between the gains measured at CERN and at Fermilab. This ratio reflects the different operating conditions (temperature and bias voltage) of the two periods.

The temperature dependence of the AHCAL response to muons was determined directly from the data collected at Fermilab. The AHCAL response to muons is described by a Landau function convolved with a Gaussian function. The mean of the Gaussian was fixed to zero. On average, 14 noise hits contributed to the total signal in the AHCAL. Subtracting the mean noise contribution (extracted from pure pedestal events) from the peak position of the convolved function yielded the most probable muon signal $\langle E^{\mu}_{\text{vis}}\rangle_0$. The requirements for selecting only events with single muons are described in Section 6.

Figure 5(a) shows $\langle E^{\mu}_{\text{vis}}\rangle_0$ for different mean detector temperatures. Only measurements with more than 250 events and where the fit of the convolved Landau function to the AHCAL response yielded a $\frac{\chi^2}{\text{NDF}}$ of less than 2 and the mean noise was less than 10 MIP are included (two third of all measurements met the $\frac{\chi^2}{\text{NDF}}$ requirement). No temperature correction procedure was applied. The squares mark the measurements that were used for extracting the muon calibration. Only measurements with a pure 32 GeV muon beam are included. The dotted line in Fig. 5(a) shows the result of fitting a line to the measurements. The linear fit yielded a slope of $-3.4\,\frac{\%}{\text{K}}$ with respect to the applied muon calibration, i.e. with respect to $\langle E^{\mu}_{\text{vis}}\rangle_0$ at 25.3 °C. The slope was used to correct the MIP calibration for temperature changes during reconstruction.

Figure 5(b) shows $\langle E^{\mu}_{\text{vis}}\rangle_0$ for different mean detector temperature for muons selected from the pion runs used for this analysis. The temperature corrections were applied. The peaks

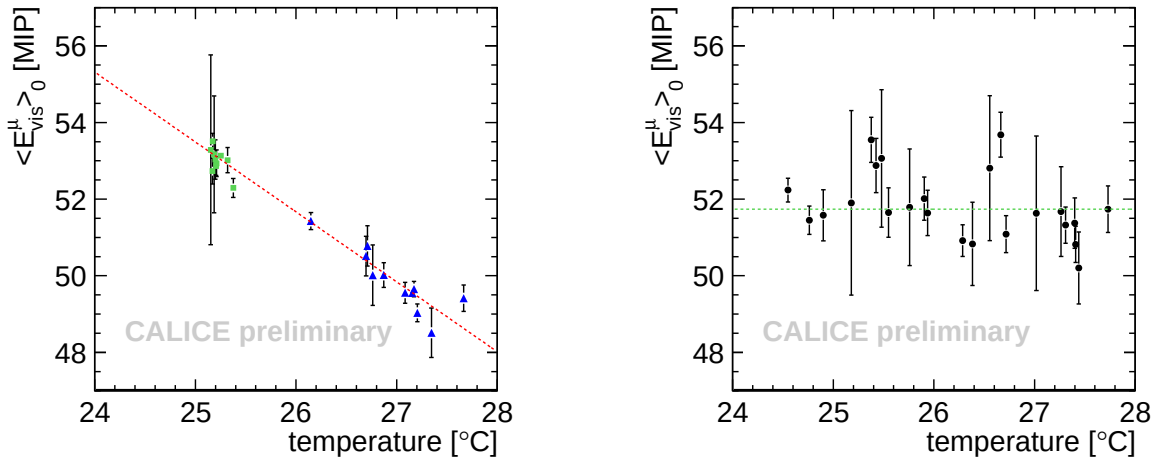

(a) (b)

Figure 5: (a) AHCAL response to muons from muon data (after subtracting the mean noise) at different detector temperatures. No temperature correction was applied. The filled squares correspond to the runs that are used for the actual muon calibration. The linear fit indicated by the dotted line yielded a relative slope of $-3.4\,\frac{\%}{\mathrm{K}}$ with respect to these measurements. (b) AHCAL response to muons measured in between pions (after subtracting the mean noise) at different detector temperatures. Temperature effects were corrected for. No remaining temperature dependence is visible, the spread of the individual measurements is 1.6%.

scatter around a line with slope 0. The spread of these values (RMS / mean) is 1.6% and is an estimate of the overall AHCAL calibration uncertainty after temperature correction. This uncertainty does not cover saturation and gain uncertainties, because they do not affect muon energy measurements.

5 Removing bad and noisy cells

Some of the 7608 cells of the AHCAL prototype were dead or noisy. Dead cells had SIPMs with bad soldering or broken connections, while noisy cells were read-out by SIPMs with long-discharge behavior. All dead and noisy cells needed to be identified and excluded from analysis. Dead cells not removed from Monte Carlo simulations could lead to different detector responses in data and in simulations. Noisy cells disturbed the homogeneity and stability of the detector response both in data and in simulations. Two types of measurements allowed for identifying these bad cells: Pedestal measurements using a random trigger and LED measurements using the LED system to illuminate all AHCAL cells with a constant amplitude. The pedestal measurements were either performed separately with 20000 events per measurement or in blocks of 500 events during the intervals between beam spills. The LED measurements were also performed in blocks of 500 events between

TABLE I
STATISTICS OF BAD CELLS.

Type	Cut	Cells
dead	$\mathrm{RMS_{ped}} < 20 \wedge \mathrm{RMS_{LED}} < 100$	204
long discharge	$\mathrm{RMS_{ped}} > 140$	22
high rate	noise rate > 0.02	55
unstable	multiple peaks	17
mean shift	$\mathrm{mean_{ped}} < -5 \vee \mathrm{mean_{ped}} > 5$	9
total		270

beam spills.

The pedestal RMS of dead cells was less than 20 ADC counts [1]. However, some of these low-noise cells showed a response to LED light. Thus, only cells with a pedestal RMS of less than 20 ADC counts and an RMS of less than 100 ADC counts during LED illumination were considered dead. For the classification of each cell, the lowest pedestal RMS and LED RMS from a series of noise and LED measurements was used. Long discharge SIPMs showed an increased pedestal width. All channels with a maximum pedestal width of more than 140 ADC counts were assigned to this group of bad cells. The noise frequency of a cell is the fraction of pedestal events in which the cell gives a signal above the 0.5 MIP threshold. Cells with a noise frequency of more than 0.02 were classified as noisy. Some channels showed pedestal shifts which resulted in multiple peaks in the pedestal histogram for a single noise measurement. The ROOT::TSpectrum [4] peak finder was used to count the number of peaks. Channels with more than one peak were considered unstable and were excluded from the analysis. Per definition, the mean pedestal of each cell after pedestal subtraction has to be at zero ADC counts. Cells for which this mean deviated by more than 5 ADC counts from zero were considered unstable as well. Table I summarizes the numbers of channels assigned to the different groups of bad cells. Appendix A provides figures illustrating the different selection criteria. The bad cells were not distributed equally over the AHCAL layers. Layers 1 (module 3) and 27 (module 30) were the layers with most bad cells (34 in layer 1 and 28 in layer 27). The number of bad cells in the other layers varied between 0 and 19. All bad and noisy cells were suppressed both for the analysis of data and Monte Carlo simulations (after digitization).

Figures 6(a) and 6(b) illustrate the improvement when excluding bad cells from analysis. Figure 6(a) shows the visible energy above the 0.5 MIP threshold (E_{vis}) in the AHCAL and Fig. 6(b) shows the mean visible energy above threshold ($\langle E_{\mathrm{vis}} \rangle$) for the individual layers of the AHCAL for pure pedestal events. The red color represents the result before and the green color after the exclusion of bad cells identified by the procedures described in this section. Excluding the noisy and unstable cells reduced the long tail in the noise distribution (dead cells do not contribute to the noise). The layer-to-layer fluctuations were due to the different SIPM production batches used to equip individual layers.

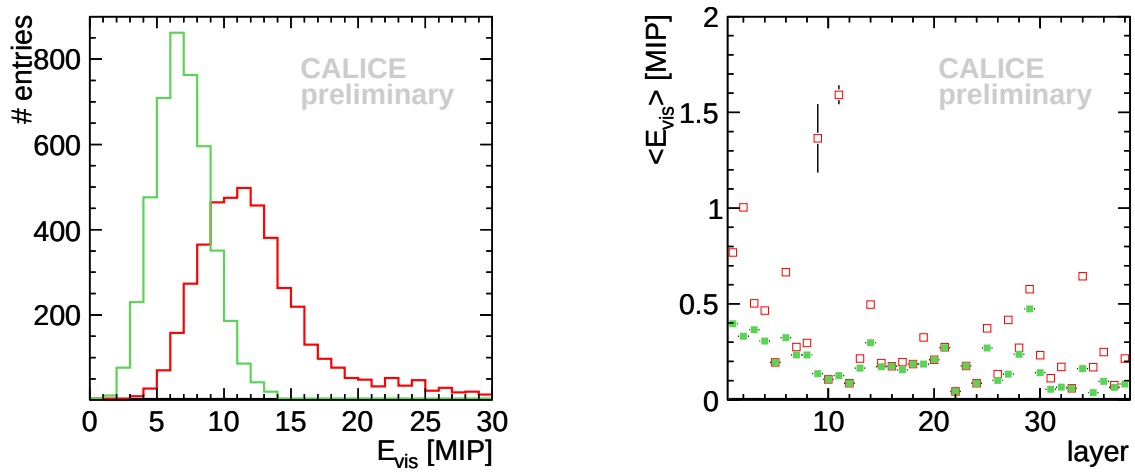

(a) (b)

Figure 6: Visible energy above threshold in the AHCAL (a) and mean visible energy above threshold for the single AHCAL layers (b). The red histogram in (a) and the open squares in (b) show the result including all cells, the green histogram in (a) and the filled squares in (b) show the result after excluding all dead, noisy and unstable cells. This noise measurement was not included in the set of measurements used for identifying the bad cells.

6 Event selection

The recorded data sets needed to be purified for analysis. This section presents basic beam quality criteria and offline selection procedures for obtaining clean electron, pion, and muon samples. Some of these criteria used information from the AHCAL itself. Applying these cuts to digitized electron and pion simulations confirmed that these cuts did not introduce any bias to the energy distributions.

The main trigger for electrons, pions, and protons was the coincidence between the signals from the two $10 \times 10\,\mathrm{cm}^2$ scintillators. Events where particles generated a beam trigger signal and were scattered away before reaching the AHCAL were rejected by requiring at least 4 MIP energy deposition in the $3 \times 3\,\mathrm{cm}^2$ cells of the first five layers of the AHCAL. About 96% of pure pedestal events had less energy in this region. Assuming pure pedestal events and spurious trigger events have the same topology (i.e. only noise), 96% of the latter events were rejected by this cut. Some events contained additional particles in the beam halo or particles that initiated a shower before reaching the AHCAL. These events were excluded by requiring no signal in the veto trigger and less than 15 hits in the $6 \times 6\,\mathrm{cm}^2$ and the $12 \times 12\,\mathrm{cm}^2$ cells of the first five AHCAL layers. In order to exclude events with more than one particle depositing energy in the AHCAL at the same time, only events with a multiplicity counter amplitude of less than 3800 ADC counts were kept for analysis. This selection corresponds to a multi-particle contamination of less than 0.1%. Figure 7 shows the signal from the multiplicity counter for one run. The

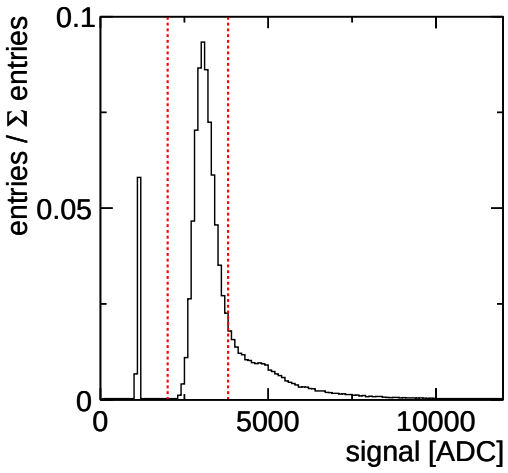

Figure 7: Signal from the multiplicity counter. The entries left of the first dashed line (2500 ADC counts) are the pedestal (no particle passing). For signals below the second dashed line (3800 ADC counts), the probability of more than one particles passing through the scintillator simultaneously is below 0.1 % [5].

entries left of the first dashed line are the pedestal (no particle passing). The second dashed line indicates the cut at 3800 ADC counts. The procedure for quantifying the multi-particle contamination is described in [5].

In order to improve the purity of the electron data, a signal in the outer Čerenkov PMT and no signal in the inner Čerenkov PMT were required. In addition, the center of gravity in beam direction had to be in the first half of the AHCAL (less than 360 mm beyond the start of the AHCAL). For 1 GeV data, only events with at least one cluster with an energy of 6 MIP or higher and less than 8 MIP energy deposited in the last 20 AHCAL layers were kept for analysis. The clusters were identified applying the algorithm described in [6]. This algorithm looks for seed hits with an energy deposition of more than 1.65 MIP and sorts them by their z-positions in ascending order. Starting with the most upstream seed hit, each seed hit and all neighboring hits are assigned to a cluster. As long as one or more of the cells added to a cluster meet the seed hit requirement, the clustering continues and all hits adjacent to these cells are assigned to the same cluster. From 2 GeV to 20 GeV, at least one cluster of 18 MIP energy or higher and less than 5 MIP energy deposited in the last 10 AHCAL layers were required. Table II summarizes all electron data used for the analysis described in this note. For all these runs, the average beam position was near the center of an AHCAL tile. Because the Čerenkov detector was also used for the online trigger decision (see Section 3), part of the Čerenkov based selection was already applied to the data before the offline selection (all events). Figures 8(a) and 8(b) present the visible energy for data collected at 1 GeV and 10 GeV beam momentum before (empty histograms) and after (filled histograms) applying the event selection for electrons. The tails to the right at both energies originate from events with an additional pion in the detector. However, these events could not be excluded with the utilisation of the multiplicity counter. The left-handed tail at 10 GeV is consistent with a small

Table II
Electron data used for this analysis.

Beam momentum	Events (selected)	Events (all)	Run
1 GeV	50991	80275	580154
2 GeV	112982	187243	580093 580102 580103
4 GeV	64333	99072	580092
6 GeV	124289	183409	580090
10 GeV	89563	138469	580087
20 GeV	63682	95921	580085

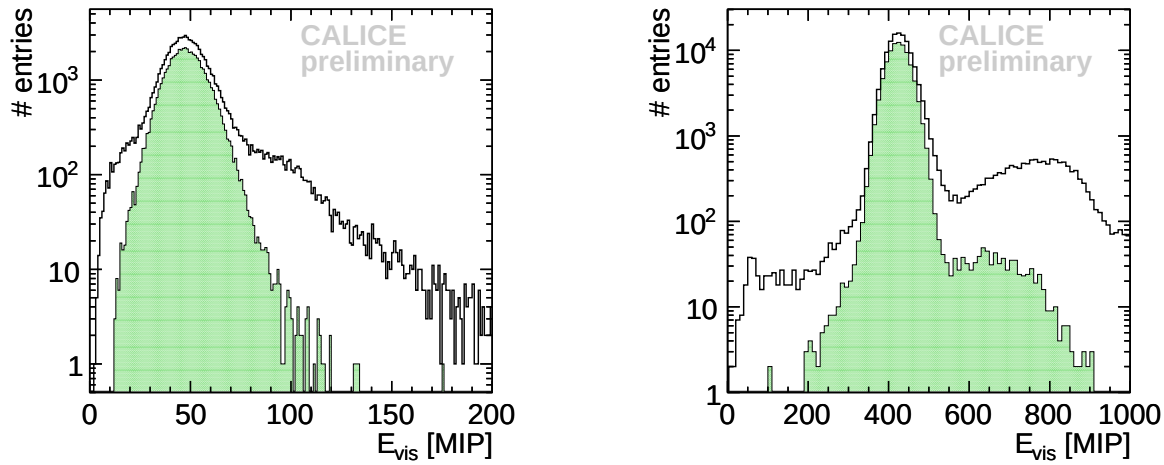

(a) (b)

Figure 8: Visible energy E_{vis} for electron measurements at 1 GeV (a) and 10 GeV (b) before (empty histograms) and after (filled histograms) applying the beam quality and electron selection criteria.

contribution from single pions.

For minimizing the electron contamination in pion data, events with a signal in the outer Čerenkov PMT were excluded. From 1 GeV to 6 GeV no signal in the inner Čerenkov PMT was required as well, while for higher beam momenta the inner PMT had to give a signal. The pion-enhanced data at all beam momenta contained a significant fraction of muon events. The efficiency of the single $1 \times 1\,\mathrm{m}^2$ scintillator behind the TCMT as a muon veto did not suffice. The efficiency was approximately 20% and was calculated as the fraction of muon events that were triggered by the $20 \times 20\,\mathrm{cm}^2$ scintillator and gave a signal in the $1 \times 1\,\mathrm{m}^2$ scintillator. In addition, low-energetic muons below 3 GeV did not reach the end of the tail catcher but were stopped in the TCMT (2 GeV) or even in the AHCAL (1 GeV). Thus, additional algorithms for identifying muon events were needed. From 1 GeV to 4 GeV, the energy in the last AHCAL layers was suited to separate pion from muon events. At 1 GeV, the energy in the last 10 layers had to be

Table III
Pion data used for this analysis.

Beam momentum	Events (selected)	Events (all)	Run
1 GeV	2472	34289	580155 580156
2 GeV	39830	155217	520291 580024 580058
4 GeV	74753	124794	580019
6 GeV	92424	162705	520305
8 GeV	55070	83457	520307
10 GeV	65797	100942	520308
12 GeV	112976	160753	520320 520321
20 GeV	64661	94366	520322
30 GeV	51199	75302	520323

below 4 MIP, at 2 GeV the energy in the last 6 layers had to be below 3 MIP and at 4 GeV the energy in the last 5 layers had to be below 5 MIP. The numbers of layers yielding the best separation between pions and muons at different beam momenta were extracted from digitized Monte Carlo simulations. At beam momenta above 4 GeV, pion showers covered the full length of the AHCAL. At these energies, an algorithm for identifying the position of the first hard interaction in the AHCAL was used to separate muon from pion events. For muon events, no such interaction occurs. The algorithm described in [6] was applied for identifying clusters from hard interactions. More than 4 hits and a minimum energy of 16 MIP in a single cluster were required. According to Monte Carlo simulations, the muon identification procedure using this algorithm worked at 6 GeV and above with muon rejection efficiencies of more than 80%. At 32 GeV, this number was confirmed by muon data. The muon contamination was reduced further by requiring more than 60 hits in the AHCAL for pion data from from 8 GeV to 30 GeV. Table III summarizes all negative pion data used for this analysis. Figures 9(a) and 9(b) present the visible energy for 1 GeV and 10 GeV beam data before (empty histograms) and after (filled histograms) applying the event selection for pions.

For collecting muon data, the coincidence between two $1 \times 1\,\mathrm{m}^2$ scintillators was used as main trigger. A clean muon beam was generated by closing the beam dump. Only muons could reach the calorimeters. In order to select single muon events for the temperature correction check described in Section 4, the following requirements were used: A track with 34-36 hits (i.e. 34-36 hits in a tower of 38 successive tiles), no hard interaction and less than 60 hits in total in the AHCAL. Because of the MIP detection efficiency of 93% and the AHCAL depth of 38 layers, muons yielded a track with 35 hits on average. The tight cut on the track length with a lower and an upper limit reduced the fluctuations of the MIP response caused by different numbers of hits contributing (1 hit difference in track length changes the response by 3%). The upper limit on the total number of AHCAL hits excluded events with additional muons.

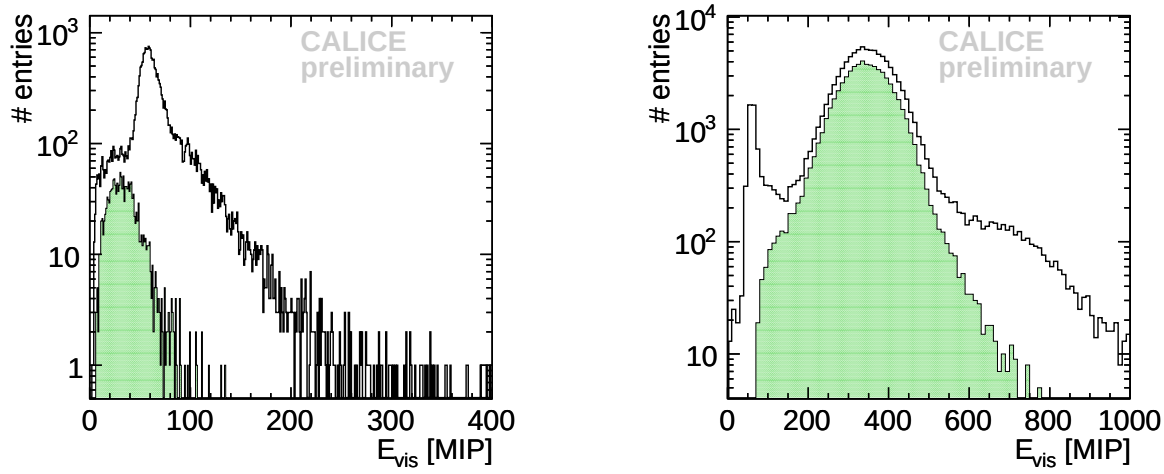

(a) (b)

Figure 9: Visible energy E_{vis} for pion measurements at 1 GeV (a) and 10 GeV (b) before (empty histograms) and after (filled histograms) applying the beam quality and pion selection criteria.

7 Data purity

The differential Čerenkov detector was used to enhance the electron or pion content in the recorded data. Because the purities of these selections were unknown, the pion contamination of the electron data and the electron contamination of the pion data needed to be estimated with the AHCAL itself.

At beam momenta above 10 GeV, electrons could be separated from pions via the correlation between the visible energy and the number of hits in the AHCAL. At lower beam momenta, the overlap of these distributions for the different particles increased significantly. An observable taking into account the different longitudinal shower shapes of electrons and pions (electron showers start earlier and are shorter than pion showers of the same energy) improved the separation of these particles at all beam momenta. Monte Carlo studies showed that the energy fraction deposited in the first five layers of the AHCAL yielded the best electron-pion separation at 1 GeV. For higher beam momenta, the separation increased.

Figures 10(a) and 10(b) show the ratio of the energy deposited in the first five AHCAL layers divided by the total measured energy for electrons (blue) and pions (green) at 1 GeV for digitized Monte Carlo simulations. The black dots in Fig. 10(a) present the electron data after applying the selection criteria from Section 6, the black dots in Fig. 10(b) present the pion data. The red curves in both figures show the result of fitting the weighted sum of the Monte Carlo distributions for both particle types to the data. The fit was performed with the ROOT:TFractionFitter [4] and yielded the best estimate for the relative contributions of the electron and pion Monte Carlo histograms to the

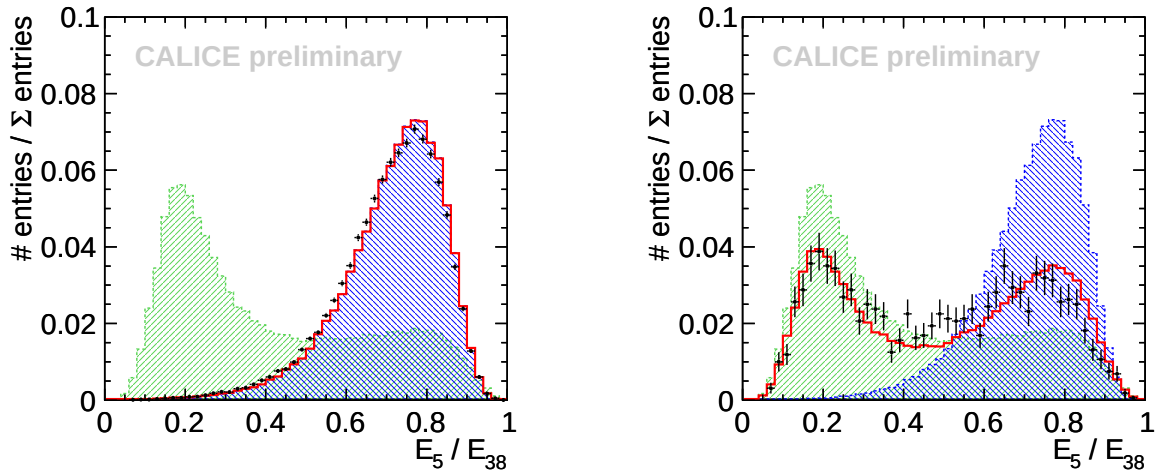

(a) (b)

Figure 10: Ratio between the visible energy in the first five AHCAL layers and all 38 AHCAL layers at 1 GeV beam momentum for pion (green) and electron (blue) simulations. The black dots show electron (a) and pion (b) data. The red line show the result of fitting the weighted sum of the simulated electron and pion histograms to the data. The electron data purity (a) is better than 99.5%, the pion data purity (b) is 71.1%.

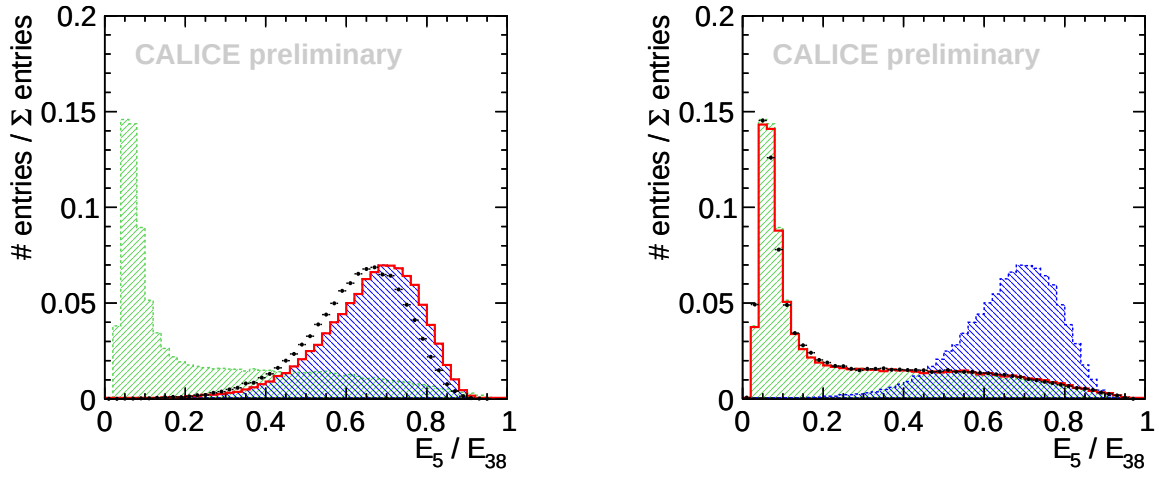

(a) (b)

Figure 11: Ratio between the visible energy in the first five AHCAL layers and all 38 AHCAL layers at 4 GeV beam momentum for pion (green) and electron (blue) simulations. The black dots show electron (a) and pion (b) data. The red curves show the result of fitting the weighted sum of the simulated electron and pion histograms to the data. The electron data purity (a) is better than 99.9%, the pion data purity (b) is 97.6%.

data histogram. The weights extracted from the fit correspond to the electron and pion content of the data. Figures 11(a) and 11(b) show the same distributions and the fit results at 4 GeV beam momentum. The electron Monte Carlo in Fig. 11(a) is shifted by 5% with respect to the electron data. This shift was also visible for electrons at higher beam momenta and is still under investigation. However, the high purity of the electron samples is clearly visible. According to the fits, the pion contamination of the electron data is less than 0.5% at 1 GeV and 0.1% or less from 2 GeV to 20 GeV. Table IV summarizes the electron contamination of the pion data. For beam momenta of 6 GeV and above, this contamination was negligible. At 1 GeV, 2 GeV and 4 GeV, the electron contamination needed to be accounted for.

TABLE IV
ELECTRON CONTAMINATION OF PION DATA.

beam momentum [GeV]	electron contamination [%]	error [%]
1	28.9	1.8
2	4.5	0.4
4	2.4	0.3
6	0.0	0.1
8	0.4	0.2
10	1.3	0.2
12	1.1	0.2
20	1.1	0.2
30	1.0	0.3

The fraction of energy deposited in the first five AHCAL layers could not be applied to separate electrons from pions on an event by event basis. Cutting on this variable introduced a strong bias and distorted the visible energy distribution, because all pions depositing their energy along a specific profile in the detector were rejected. However, knowing the amount of electron contamination of the pion data allowed for statistically subtracting the electron contribution from all analyzed distributions. Figure 12(a) presents the visible energy for the full pion data set at 1 GeV (black) and the visible energy for electrons weighted by the relative electron contamination from Table IV (blue). The red histogram shows the difference between the other two histograms. The resulting histogram is the real distribution for pions after subtracting the electron contribution and was used for further analysis. Figure 12(b) shows the same for 2 GeV data. This procedure was applied to the 4 GeV pion data as well.

8 Analysis results

8.1 Electron data

Figure 13(a) presents the measured visible energy E^e_{vis} for electrons at different beam momenta and Gaussian fits applied to the central 90% of the statistics. The Gaussians

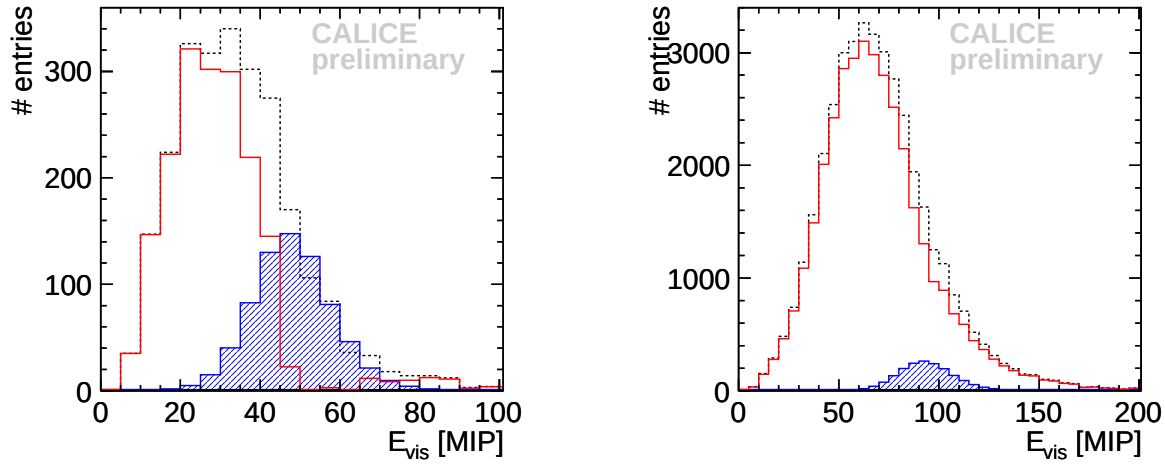

(a) (b)

Figure 12: Statistical subtraction of electron contamination from visible pion energy for pion data at 1 GeV (a) and 2 GeV (b) beam momentum. The dotted lines present the pion data with electron contamination, the shaded histograms show electron data scaled to the contamination fractions from Table IV, the solid blank histogram shows the difference between the two histograms.

describe the histograms well. From these fits, mean $\langle E^e_{\rm vis}\rangle$ and sigma $\sigma^e_{\rm vis}$ of the visible energy for electrons were extracted. The mean noise above threshold in the full AHCAL was about 7 MIP and corresponded to less than 1% of the signal at 20 GeV and 15% of the signal at 1 GeV. The noise introduced an offset to the energy scale and had to be reduced in order to obtain a linear detector response. One approach is to define a fiducial volume which covers only part of the detector. This approach is followed in [2]. Another option is to subtract the mean noise from the mean visible energy. The drawback of this second method is that the noise contribution to the signal width is not reduced. However, the advantage is that this method can be applied to pions as well where the definition of a fiducial volume covering all signal cells is more difficult than for electrons. For this analysis, the second option was chosen. The mean noise was extracted from pure pedestal events collected in between beam events. Figure 13(b) shows the mean visible energy $\langle E^e_{\rm vis}\rangle_0$ after subtraction of the mean noise for beam momenta $p_{\rm beam}$ from 1 GeV to 20 GeV. A linear fit $\left(\langle E^e_{\rm vis}\rangle_0[\text{MIP}] = p_{\rm beam}[\text{GeV}]\cdot w[\frac{\text{MIP}}{\text{GeV}}]\right)$ was performed on these data. The fit yielded a conversion factor w from MIP to GeV of $(41.7\pm0.3)\,\frac{\text{MIP}}{\text{GeV}}$. For the CERN data, a factor of $(42.3\pm0.4)\,\frac{\text{MIP}}{\text{GeV}}$ was obtained [2]. Using an alternative fit function $\left(\langle E^e_{\rm vis}\rangle_0^{alt} = p_{\rm beam}\cdot w^a + c^a\right)$ for the Fermilab data yielded $w^a = (42.0\pm0.4)\,\frac{\text{MIP}}{\text{GeV}}$ and $c^a = (-0.6\pm0.8)$ GeV. All results agree within errors.

Figure 14(a) presents both the reconstructed energy ($E^e_{rec} = \langle E^e_{vis}\rangle_0/w$) from the Fermilab electron measurements and the CERN positron measurements [2]. The combined data sets cover the energy range from 1 GeV to 50 GeV. The dashed line indicates the equality between beam momentum and reconstructed energy. Figure 14(b) shows the deviation

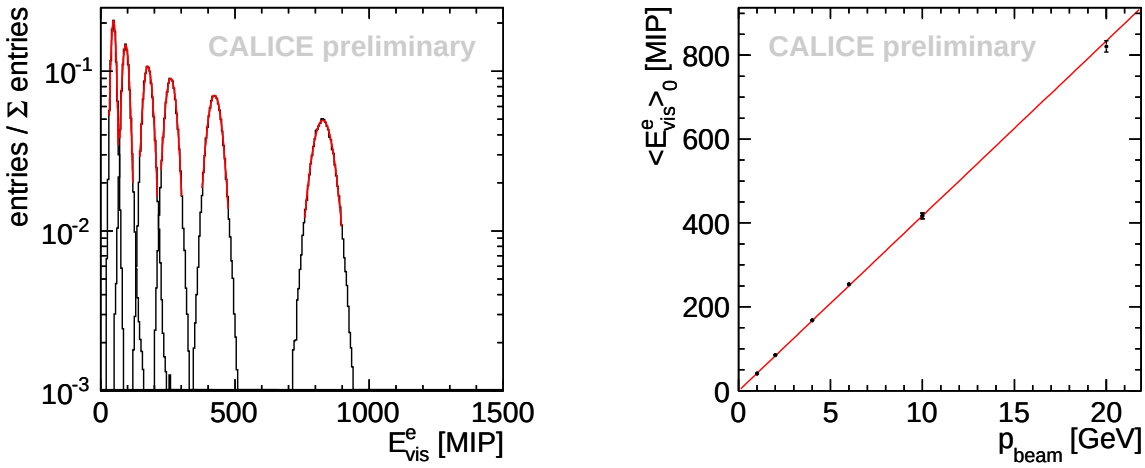

(a) (b)

Figure 13: (a) Visible energy for electrons (beam momenta in GeV, from left to right: 1, 2, 4, 6, 10 and 20). The red lines are the results of the Gaussian fits applied to the central 90% of the statistics. (b) Difference between mean visible energy and mean noise above threshold. A linear fit (solid line) performed on these data yields $w = (41.7 \pm 0.3)\,\frac{\mathrm{MIP}}{\mathrm{GeV}}$.

of the reconstructed energy from the beam momentum. The Fermilab data confirm the detector linearity for electrons down to 1 GeV. An uncertainty of 3% was assumed for the beam momentum [7].

Figure 15 shows the detector resolution $\frac{\sigma_e}{E_e}$ for electrons from this analysis $\left(\frac{\sigma_e}{E_e} = \frac{\sigma^e_{vis}}{\langle E^e_{vis}\rangle_0}\right)$ and positrons (CERN 2007, [2]) at different beam momenta. The resolution is the width of the visible energy divided by the visible energy after subtracting the mean detector noise. For the Fermilab data, a beam momentum uncertainty of 3% was assumed [7]. The detector resolution is described by

$$\left(\frac{\sigma}{E}\right)^2 = \left(\frac{a}{\sqrt{E}}\right)^2 + \left(\frac{b}{1}\right)^2 + \left(\frac{c}{E}\right)^2 . \tag{3}$$

The parameter a is the stochastic term, b is the calibration related term, and c is the constant noise term. Estimating the noise term c from pure pedestal events yielded $c = 50\,\mathrm{MeV}$. The fit of function (3) to the Fermilab data (fixing $c = 50\,\mathrm{MeV}$) is presented in Fig. 15 as well (solid line). The dashed line is the extension of the fit to higher energies. Table V summarizes the fit parameters and their uncertainties for the electron data from Fermilab and the positron data from CERN [2]. Varying the fixed noise term from $c = 0\,\mathrm{MeV}$ to $c = 70\,\mathrm{MeV}$ only changed the results of the remaining fit parameters within their errors. A combined fit to the data from both measurement periods yielded compatible values. The results agree within their uncertainties.

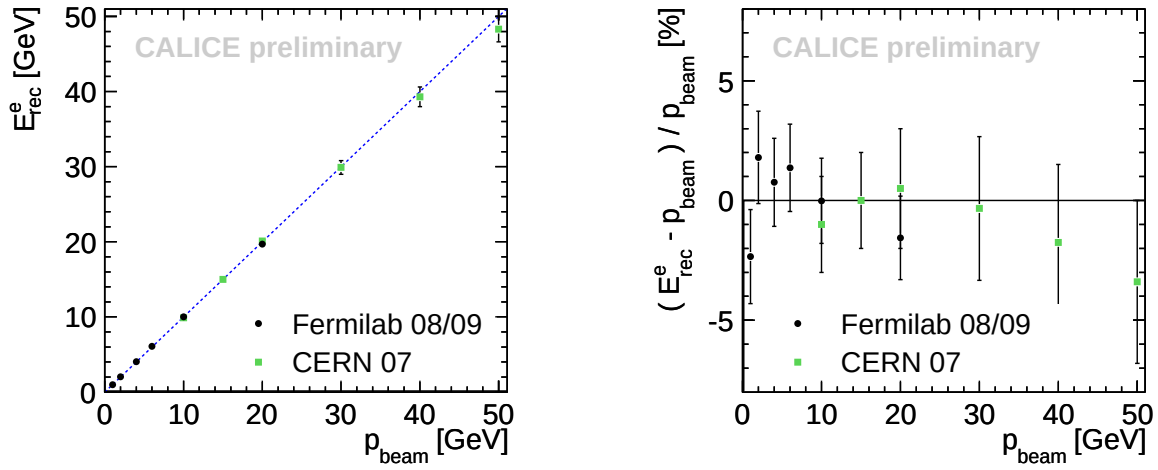

(a) (b)

Figure 14: (a) Mean reconstructed electron (positron) energy at different beam momenta. A MIP/GeV conversion factor of $(41.7 \pm 0.3)\,\frac{\text{MIP}}{\text{GeV}}$ (CERN: $(42.3 \pm 0.4)\,\frac{\text{MIP}}{\text{GeV}}$) is applied to calibrate the energy measurements from Fermilab (CERN) to the GeV scale. The dashed line indicates a linear response ($E^e_{rec} = p_{beam}$). (b) Deviation between the measured energy and the beam momentum.

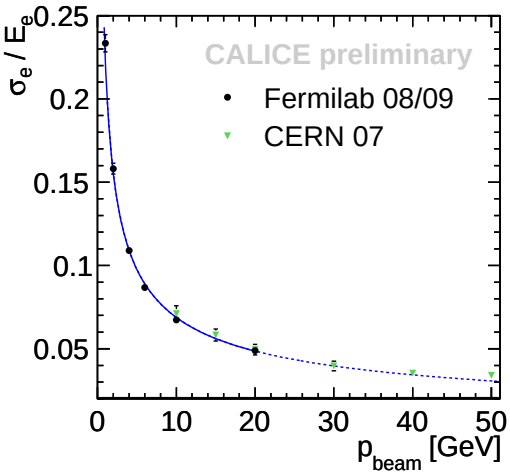

Figure 15: AHCAL resolution for electrons (black circles, Fermilab data) and positrons (green triangles, CERN data from [2]). The solid line presents the fit of Eq. (3) to the electron data, the dotted line is the extension of the fit result to higher beam momenta.

TABLE V
AHCAL ELECTRON / POSITRON RESOLUTION.

parameter	Fermilab	error	CERN	error
a	21.7%	0.2%	21.9%	1.4%
b	0.0%	0.8%	1.0%	1.0%
c	50 MeV	-	58 MeV	-

8.2 Pion data

Figure 16 shows the visible energy E^{π}_{vis} for the negative pion data measured at beam momenta from 1 GeV to 30 GeV. The electron contamination after event selection was subtracted statistically for 1, 2 and 4 GeV (see Section 7). The red lines indicate the results of performing Gaussian fits to the central 70% of the statistics. Restricting the fit range excluded the tails of the distributions. The tails to the left increase with higher beam momenta due to an increased fraction of pion showers leaking to the tail catcher. In the current analysis, no attempt to recover the leaked energy was made. The fits yielded mean ($\langle E^{\pi}_{\text{vis}} \rangle$) and sigma of the energy measurements. From these means, the mean noise above threshold was subtracted. The differences ($\langle E^{\pi}_{\text{vis}} \rangle_0$) were converted from the MIP to the electromagnetic GeV scale via $E^{\pi}_{\text{rec}}(\text{EM-scale}) = \langle E^{\pi}_{\text{vis}} \rangle_0 \ / \ w$, where $w = (41.7 \pm 0.3) \frac{\text{MIP}}{\text{GeV}}$ is the electromagnetic conversion factor (see Section 8.1). Figure 17(a) shows the reconstructed pion energy at the electromagnetic scale for different beam momenta. We expect a non-linear detector response to pions. This non-linearity is attributed to the energy dependence of the electromagnetic fraction in hadron showers. The AHCAL response to the hadronic shower component is smaller than the response to the electromagnetic shower component. The $\frac{\pi}{e}$ ratio (i.e. the ratio between the detector response to pions and electrons of the same momentum) expresses this effect. Figure 17(b) presents the $\frac{\pi}{e}$ ratio ($\langle E^{\pi}_{\text{vis}} \rangle_0 \ / \ \langle E^{e}_{\text{vis}} \rangle_0$) for the data collected at Fermilab at beam momenta from 1 GeV to 20 GeV. The ratio is smaller than 1 and increases for higher beam momenta.

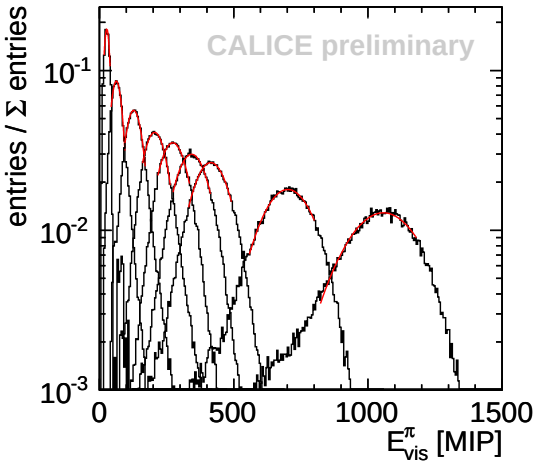

Figure 16: Visible energy for pions (beam momenta in GeV, from left to right: 1, 2, 4, 6, 8, 10, 12, 20 and 30). The red lines are the results of the Gaussian fits applied to the central 70% of the statistics.

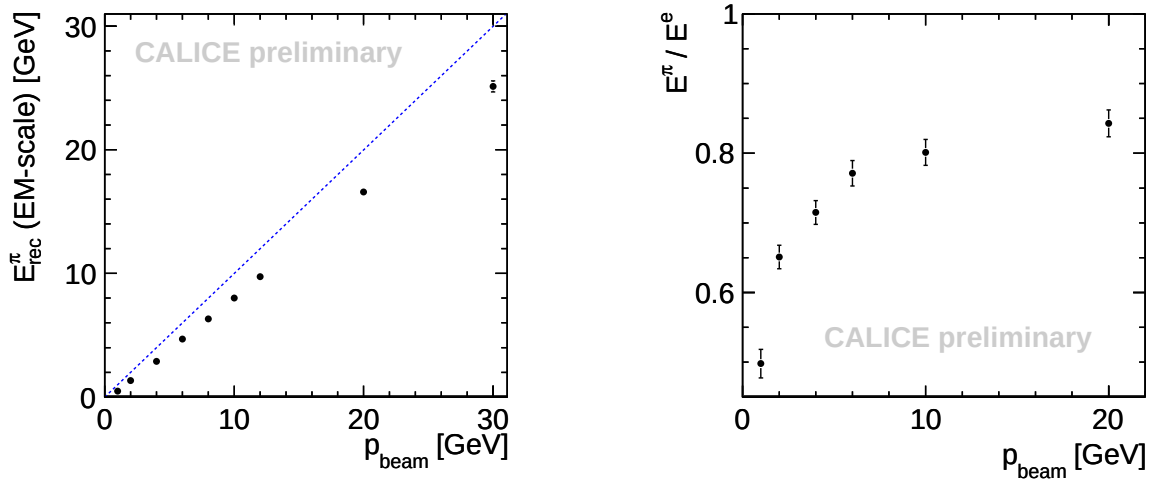

(a) (b)

Figure 17: (a) Mean reconstructed pion energy at different beam momenta. A MIP/GeV conversion factor of $(41.7 \pm 0.3)\,\frac{\text{MIP}}{\text{GeV}}$ is applied to calibrate the energy measurements to the electromagnetic scale. The dashed line indicates a linear response ($E^{\pi}_{rec} = p_{beam}$). (b) Ratio between the mean energy measured for pions and electrons (at the same beam momentum) for different beam momenta.

9 Summary

From 2008 to 2009, the AHCAL was successfully operated at the Fermilab Test Beam Facility. The electron and pion data collected with the AHCAL during these measurements are a valuable extension to earlier data sets. The electron data cover the range from 1 GeV to 20 GeV, the pion data cover the range from 1 GeV to 30 GeV. During this operation, a differential Čerenkov detector was used to significantly enhance the content of electrons or pions in the recorded data sets.

The calibration of the AHCAL included a correction for the temperature dependent behavior of the SIPMs. After taking into account these corrections, the total calibration uncertainty was about 1.6% (not including uncertainties from the saturation correction). The identification and exclusion from analysis of 270 dead, noisy and unstable cells improved the homogeneity and stability of the AHCAL response. The event selection procedures presented in this note yielded electron samples with purities above 99.9% from above 1 GeV and about 99.5% at 1 GeV. The remaining electron contamination of the pion data at 1, 2 and 4 GeV after applying the event selection criteria for pions was subtracted statistically from the analysed distributions.

The electron data cover the range from 1 GeV to 20 GeV. The analysis of these data yielded a MIP/GeV conversion factor of $(41.7 \pm 0.3)\,\frac{\mathrm{MIP}}{\mathrm{GeV}}$. Within uncertainties, the linearity of the AHCAL in the covered energy range was confirmed. The resolution extracted from these data has a stochastic term of $(21.7 \pm 0.2)\,\%/\sqrt{\mathrm{E[GeV]}}$ and a constant term of $(0.0 \pm 0.8)\,\%$. All these results agree with the results obtained from the positron data recorded at CERN in Summer 2007 between 10 GeV and 50 GeV beam momenta.

The analysis of pion data yielded a $\frac{\pi}{e}$ factor of 0.5 at 1 GeV and 0.85 at 20 GeV. These data will provide the basis for future comparisons between data and Monte Carlo simulations.

References

[1] CALICE Collaboration, C. Adloff *et al.*, "Construction and Commissioning of the CALICE Analog Hadron Calorimeter Prototype", JINST **5** (2010) P05004.

[2] CALICE Collaboration, C. Adloff *et al.*, "Electromagnetic response of a highly granular hadronic calorimeter", JINST **6** (2011) P04003.

[3] `http://www-ppd.fnal.gov/FTBF/`

[4] R. Brun *et al.*, "ROOT Data Analysis Framework", `http://root.cern.ch/`

[5] B. Lutz, "Hadron showers in a highly granular calorimeter", DESY-THESIS-2010-048.

[6] CALICE Collaboration, "Preliminary results from hadron shower data with the CALICE tile AHCAL prototype – Addendum D", CALICE Analysis Note CAN-011 Appendix D (2009).

[7] E. Ramberg, "A broad energy range detector test beam facility at Fermilab", Presented at 2007 IEEE Nuclear Science Symposium and Medical Imaging Conference (NSS MIC 2007), Honolulu, Hawaii, 28 Oct - 3 Nov 2007, `DOI 10.1109/NSSMIC.2007.4436616`

[8] C. Leroy and P. Rancoita, "Physics of cascading shower generation and propagation in matter: Principles of high-energy, ultrahigh-energy and compensating calorimetry", Rept. Prog. Phys. **63** (2000) 505.

A Additional material: Bad cell selection

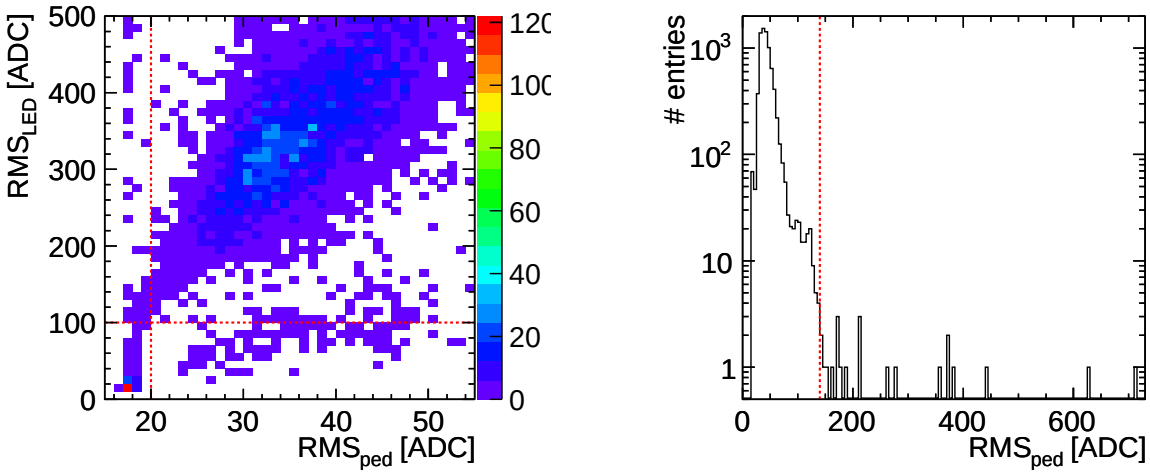

(a) (b)

Figure 18: (a) Minimum RMS for each channel from a series of pedestal measurements ($\mathrm{RMS_{ped}}$) and minimum RMS from a series of LED measurements ($\mathrm{RMS_{LED}}$). Cells with $\mathrm{RMS_{ped}} < 20$ and $\mathrm{RMS_{LED}} < 100$ are considered dead. (b) Maximum RMS for each channel from a series of pedestal measurements. Cells with $\mathrm{RMS_{ped}} > 140$ are rejected.

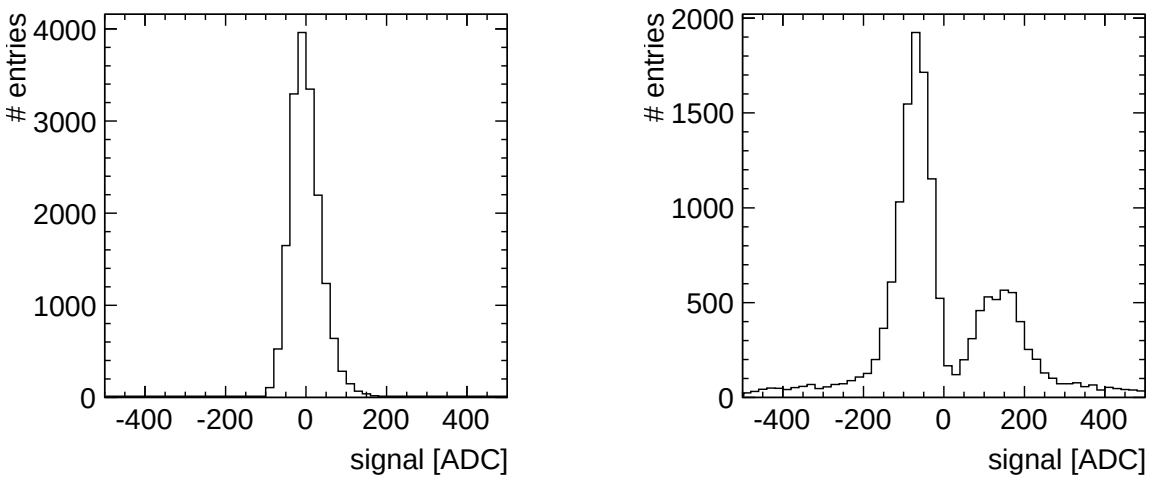

(a) (b)

Figure 19: The pedestal after subtracting the mean pedestal for a good cell with a single peak (a) and an unstable cell with two peaks (b).

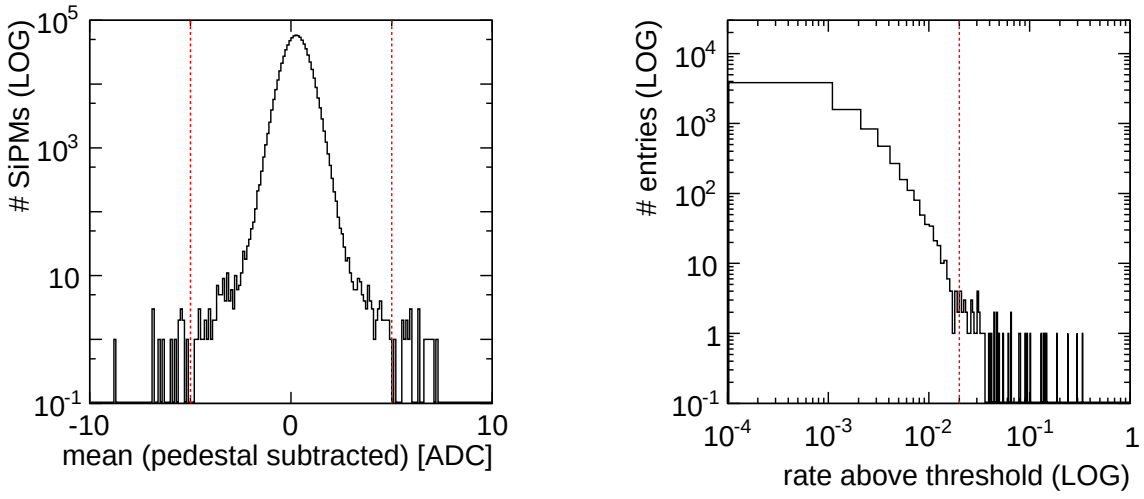

(a) (b)

Figure 20: (a) Deviation of the mean pedestal from zero (after subtracting the mean of a subset of the events from same measurement). Each entry corresponds to the maximum deviation found for one AHCAL channel in a series of pedestal measurements. Cells with mean < -5 or mean > 5 were considered unstable. (b) Total noise hit frequency above 0.5 MIP threshold for all cells combining a series of pedestal measurements. All cells with a noise frequency above 0.02 were excluded from analysis.